Nanoscale Advances

ROYAL SOCIETY OF CHEMISTRY

PAPER

View Article Online
View Journal | View Issue

Cite this: *Nanoscale Adv.*, 2025, **7**, 7726

Morphology-driven electrochemical properties of nickel-hydroxide and performance of asymmetric button-cell hybrid device

Xiaolong Leng, †[a] Jie Zeng,†[b] S. V. Prabhakar Vattikuti,*[b] Jaesool Shim,*[b] Thanh Liem Huynh *[cd] and Nam Nguyen Dang [cd]

Received 17th May 2025
Accepted 11th September 2025

DOI: 10.1039/d5na00488h

rsc.li/nanoscale-advances

Nickel-hydroxides have garnered significant attention for energy storage applications owing to their unique interfacial characteristics and tunable structural properties. Despite this potential, precise morphological control of 3D/2D nanostructures remains a major challenge. In this study, we report a morphology-directed synthesis of nickel hydroxide (NH) nanostructures using two different halogen-containing precursors: ammonium iodide (AI) and ammonium chloride (ACl). The resulting AI-NH and ACl-NH samples exhibit distinct morphologies and physicochemical characteristics, influenced by the nature of the halide ions. Their electrochemical performance was systematically evaluated using both three-electrode and asymmetric button-cell configurations. Among the two electrodes, the ACl-NH electrode achieved a higher specific capacity of 795 C g^{-1} at 1.5 A g^{-1}, compared to 601.5 C g^{-1} for AI-NH, and retained 97% of its capacity over 6000 cycles at 24 A g^{-1}. This improvement is attributed to the increased surface area of ACl-NH (16.3 m^2 g^{-1}) *versus* AI-NH (9.58 m^2 g^{-1}). Furthermore, a asymmetric device assembled with AI-NH and ACl-NH electrodes delivered a specific capacitance of 106.5 F g^{-1} at 1.5 A g^{-1}, an energy density of 37.8 Wh kg^{-1} at a power density of 1975.3 W kg^{-1}, and maintained 78% capacity retention over 8500 cycles.

1. Introduction

The growing global demand for sustainable energy solutions has intensified the search for efficient energy storage technologies. Among these, supercapacitors have emerged as promising candidates due to their rapid charge–discharge capability, high power density, and long cycle life, making them ideal for applications such as electric vehicles and portable electronics.[1,2] Their performance is largely governed by the choice of electrode material, which directly influences energy storage mechanisms and charge transport efficiency.[3]

Nickel-based layered double hydroxides (LDHs), particularly nickel hydroxide (NH), are widely studied pseudocapacitive materials owing to their high theoretical capacitance and fast redox kinetics involving the Ni^{2+}/Ni^{3+} transition.[4,5] However, the practical application of NH is often hindered by limitations in electrical conductivity and sluggish ion diffusion. Recent research suggests that these challenges can be addressed by tailoring the material's morphology to enhance surface area, electrolyte accessibility, and electron pathways.[6–8] Tran *et al.*[9] synthesized flower-like NiO *via* a hydrothermal method using nickel nitrate and urea, followed by calcination. By adjusting the Ni-to-urea ratio, solvent system, and adding CTAB, they achieved uniform particles with a high surface area (62.97 m^2 g^{-1}). Ethanol reduced ion diffusion, while CTAB regulated particle growth, enhancing structural uniformity. Hoque *et al.*[10] highlighted that the solvent conditions and pH significantly influence precursor solubility, ion diffusion, and ultimately the morphology of NH nanoparticles, producing forms like spheres or plates. Ping *et al.*[11] further demonstrated that controlling the spin state of Ni^{2+} enables the growth of large 2D α-NH crystals. These findings suggest that optimizing synthesis parameters, such as solvent type, pH, and precursor selection, can enhance surface area, ion mobility, and electrochemical performance, offering a strategic route for designing advanced nanomaterials for energy uses.

Recent synthesis methods like hydrothermal and sol–gel techniques enable precise control over NH morphology.[12,13] Templating approaches help form porous structures that enhance ion transport, while incorporating conductive materials such as graphene or carbon nanotubes improves electrode conductivity and supercapacitor performance.[14] Liu *et al.*[15]

[a]*School of Mechanical Engineering, Hubei Engineering University, Xiaogan 432000, China*

[b]*School of Mechanical Engineering, College of Engineering, Yeungnam University, Gyeongsan 38541, Republic of Korea. E-mail: vsvprabu@gmail.com; jshim@ynu.ac.kr*

[c]*Future Materials & Devices Lab, Institute of Fundamental and Applied Sciences, Duy Tan University, Ho Chi Minh City 70000, Vietnam. E-mail: huynhthanhliem@duytan.edu.vn*

[d]*The Faculty of Environmental and Chemical Engineering, Duy Tan University, Danang 55000, Vietnam*

† Authors equally contributed.

designed a 3D MnCo-LDH@NH core–shell structure on nickel foam, achieving high durability and a capacitance of 2320 F g^{-1} at 3 A g^{-1}. Yan *et al.*[16] synthesized flower-like NH on graphene *via* a microwave-assisted method, forming an asymmetric device that delivered 218.4 F g^{-1} and 77.8 Wh kg^{-1} at 1.6 V, with 94.3% retention over 3000 cycles. These studies emphasize the critical role of morphology in enhancing electrochemical performance, a key focus of the present work.

Despite ongoing advances, the influence of halogen-based precursors on the morphology and electrochemical performance of NH remains underexplored. This study aims to fill that gap by synthesizing 3D/2D structured nickel hydroxides using two different halogen precursors ammonium iodide (AI) and ammonium chloride (ACl) *via* hydrothermal methods. By comparing the resulting structural, surface, and electrochemical properties of AI-NH and ACl-NH, this research offers insight into how halogen-mediated morphology control can optimize NH-based electrodes for high-performance energy storage devices.

2. Experimental details

2.1 Preparation procedure of NH

Initially, nickel hydroxide (NH) was synthesized using different halogens (Cl, I) through the following procedure: 4 mM of $Ni(NO_3)_2 \cdot 6H_2O$ was dissolved in deionized H_2O, followed by stirring. Next, 6 mM of either ammonium iodide (AI) or ammonium chloride (ACl) and urea were added at 5 minute intervals over 20 minutes. The resulting pale-green solution was then moved into Teflon-cased autoclaves and maintained at 160 °C for 10 hours. After cooling to 25 ± 1 °C, the obtained powders were collected, thoroughly washed with ethanol and water, and dried at 80 °C overnight for further characterization. The samples were labeled as AI-NH and ACl-NH. Fig. 1 illustrates the schematic representation of the AI-NH and ACl-NH materials. The experimental procedures, electrochemical analysis, and device fabrication details are provided in the SI file.

3. Results and discussion

3.1 Structure and morphology

The α-NH structure exhibits wider interlayer spacing, with diffraction peaks at lower angles (approximately $2\theta = 12°$), while β-NH has narrower interlayer spacing, characterized by a primary (001) diffraction peak near $2\theta = 19°$.[17,18] The diffraction peaks of α-NH are broader and weaker due to its disordered structure, especially in the high-angle region. In contrast, β-NH displays sharper and more intense peaks, reflecting a highly ordered crystalline structure with larger grain sizes. Fig. 2(a) reveals that the diffraction peaks are sharper and more intense for β-NH, with multiple peaks clearly visible in the high-angle region (33°, 38°, 52°, 59°).[17–19] As the 2θ angle increases, additional diffraction peaks become evident at 2θ = 33°, 38°, 52°, 59°, and 62°, corresponding to the (100), (101), (102), (110), and (111) facets, respectively. This indicates a higher degree of crystallinity and a more regular hexagonal crystalline structure for β-NH. The absence of interspersed water molecules or anions between its layers contributes to its orderly and symmetric arrangement. These well-defined peaks confirm the regular stacking within the crystal structure and the high degree of crystallinity in β-NH.

The FTIR data in Fig. 2(b) reveal a distinct prominence of the two peaks at approximately 530 cm^{-1} and 3640 cm^{-1}, as evident from the analysis. The vibrational peak near 530 cm^{-1} is usually credited to the stretching vibration of the Ni–O bond,[20] and variations in its intensity/width mainly reflect differences in crystallinity, nanosheet thickness/orientation, and defect density between ACl-NH and AI-NH; they should not be interpreted as direct halide-induced strengthening of intrinsic Ni–O bonds. The sharp O–H stretching band observed near ~3640 cm^{-1} indicates relatively weak hydrogen bonding, as strong hydrogen-bonding interactions would broaden the band and shift it to lower wavenumbers.[21] This peak is also present in materials with I-precursors, but its intensity is usually weaker and the peak shape broader, indicating more defects in the

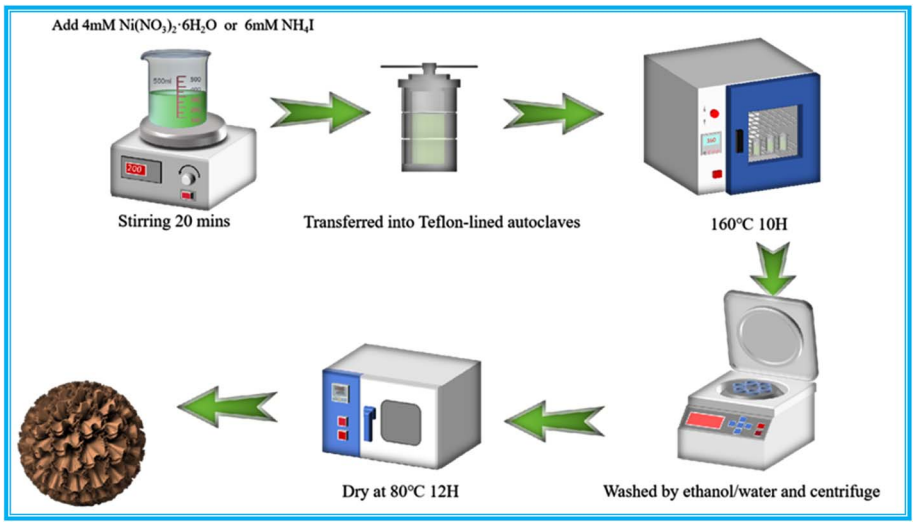

Fig. 1 Schematic representation of the synthetic procedure of AI-NH and ACl-NH materials.

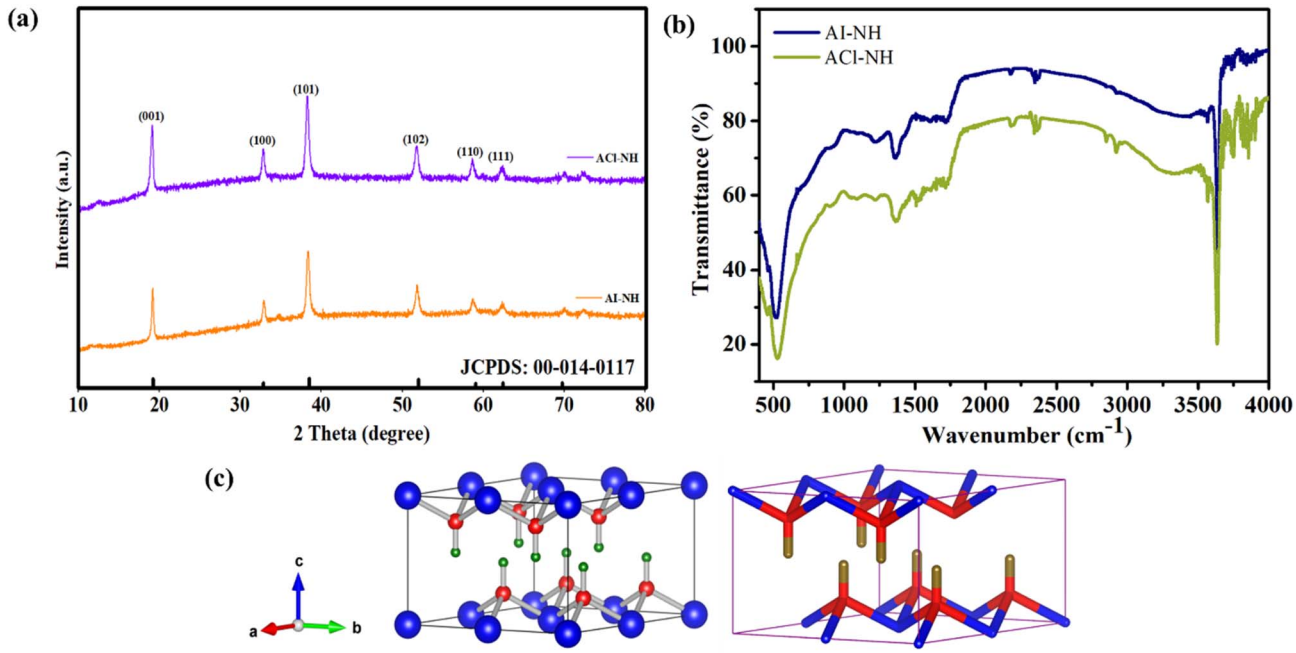

Fig. 2 (a) XRD profiles and (b) FTIR spectra of AI-NH and ACl-NH sample; and (c) molecular structure of NH materials.

crystal structure of the AI-NH. The peak located at 1362 cm^{-1} corresponds to the surface carbonate/residual nitrate while the H–O–H bending mode of interlayer/adsorbed water typically appears near ~1630 cm^{-1}. Fig. 2(c) provides a comprehensive illustration of the molecular structures of the NH materials, emphasizing the arrangement and connectivity of nickel and hydroxide ions within the framework. The depiction reveals the layered structure characteristic of NH, where nickel ions are coordinated with hydroxide ions, forming a stable and orderly lattice. This molecular arrangement is significant as it determines the material's properties, such as its ability to facilitate ion exchange, electrical conductivity, and surface reactivity.

A thorough examination of the SEM images (Fig. 3) and elemental mapping highlights the structural characteristics of the samples. The AI-NH sample (Fig. 3(A)) exhibits a nanoflower-like structure characterized by layered, flaky sheets that are loosely packed and interconnected. These sheets display sharp edges and irregular stacking, with surface features such as wrinkles and folds, which potentially increase the availability of active sites. In contrast, the ACl-NH sample (Fig. 3(B)) reveals a compact, flower-like morphology, showcasing a hierarchical arrangement with layers densely clustered into spherical formations. This structure is notably more cohesive and denser compared to AI-NH, suggesting reduced porosity but improved mechanical durability. The spherical clusters also display well-defined boundaries, indicating consistent particle size and material distribution. Additionally, the porosity, visible as gaps between the layers, offers potential pathways for enhanced mass transfer and diffusion. The SEM mapping and elemental analysis (Fig. 3(A) and (B)) provides a detailed comparison of the nickel content in the two samples, highlighting significant variations.

The HRTEM images and associated elemental mapping (Fig. 4(a–e)) of the ACl-NH sample reveal the presence of numerous nanoscale protrusions on the surface. The HRTEM images display a distinct fibrous or needle-like morphology, forming a highly interconnected network. These protrusions not only increase the material's specific surface area but also improve its wettability within electrolytes, thereby enhancing its specific capacity. Fig. 4(f) presents the SAED pattern, which displays distinct dot patterns indicative of the sample's crystalline nature. This observation is further supported by the broad peaks observed in the XRD analysis, confirming the material's crystallinity. Elemental mapping (Fig. 4(g–l)) further validates the uniform distribution of essential elements, including nickel, within the nanostructure. This homogeneous dispersion suggests successful incorporation of these elements, with the dense, fibrous features observed in the HRTEM likely corresponding to regions with higher nickel concentration, thereby enhancing the material's functional performance.

Based on the XPS data presented in Fig. 5(a), the presence of nickel (Ni) and oxygen (O) elements can be discerned, while further analysis of individual peaks of the β-NH structure. The Ni 2p spectra of β-NH typically exhibit two prominent peaks, namely Ni $2p_{3/2}$ and Ni $2p_{1/2}$, with binding energies approximately located at 855 eV and 872 eV (Fig. 5(b)), respectively.[22,23] The primary peak corresponding to Ni $2p_{3/2}$ manifests the characteristic features of Ni^{2+}, while the shoulder peaks or satellites arise from shake-up satellites and multiplet splitting, commonly observed around 860 eV and 879 eV (Fig. 5(b)).[23] The main O 1s peak for β-NH typically occurs at approximately 530 eV (Fig. 5(c)), indicating the presence of Ni–O bonds. The composition of the material can be further confirmed by comparing the relative intensities and positions of the Ni 2p

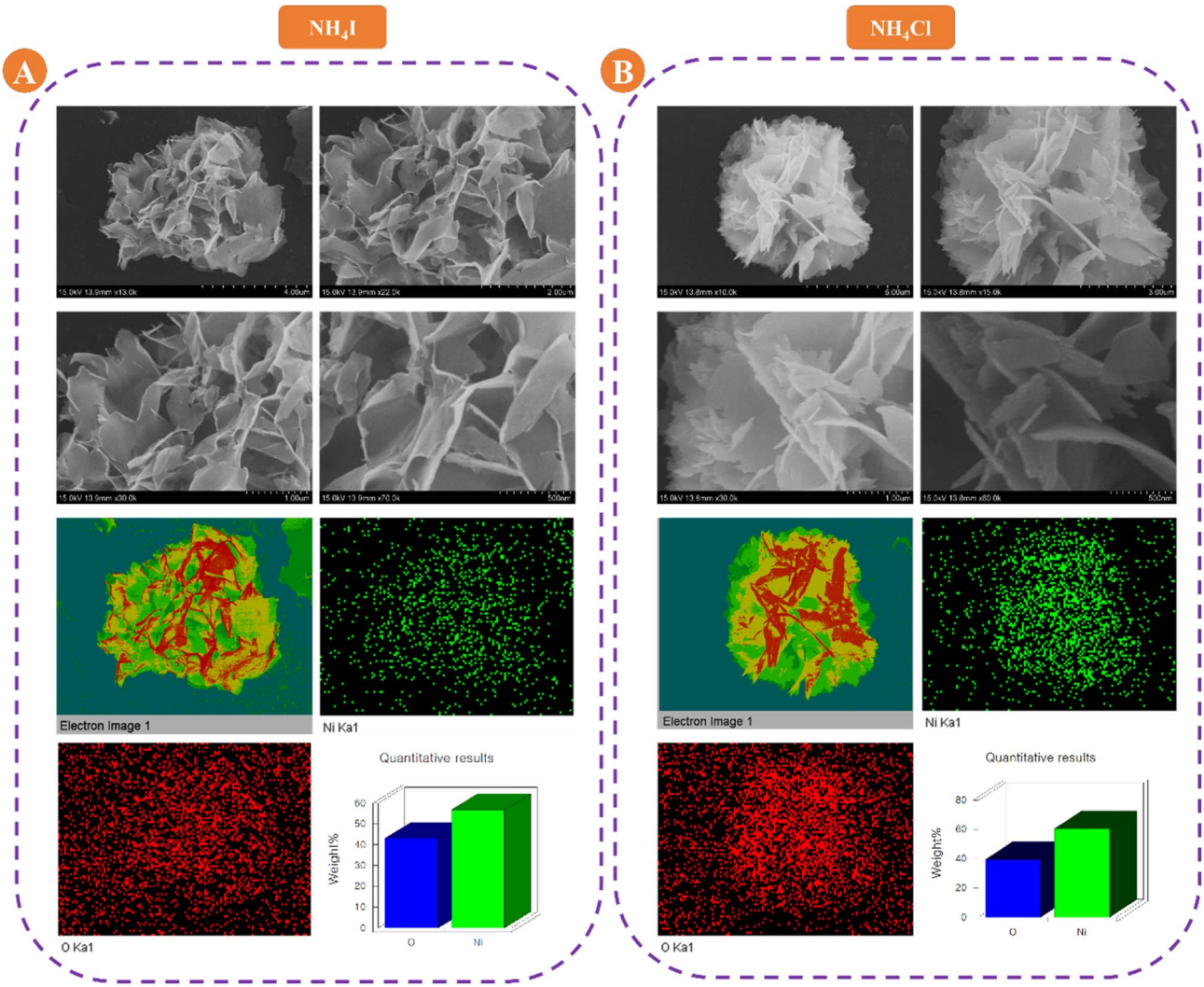

Fig. 3 FESEM images of AI-NH (A) and ACl-NH (B) samples.

and O 1s peaks. Additionally, quantifying the atomic percentages of Ni and O using XPS spectroscopy reveals a close to 1 : 2 ratio, confirming that the Ni–O/OH surface chemistry.

3.2 Formation mechanism of AI-NH and ACl-NH nanoflowers

The morphology of the β-NH nanoflower structure is notably influenced by the introduction of Cl^- and I^- ions, as these halogens present as counter-ions in the precursor/solution and act as growth-directing species during the synthesis process. SEM imaging reveals that ACl-NH displays a more aggregated nanoflower morphology, whereas AI-NH exhibits a relatively dispersed structure. This distinction is attributed primarily to differences in halide–Ni^{2+} complexation strength, facet-selective adsorption, and ionic-strength effects during nucleation and growth Chlorine ions (Cl^-) have a smaller ionic radius (~1.81 Å) and higher electronegativity (3.16), acting in solution and at crystal surfaces. This surface mediation promotes the formation of a tightly packed nanoflower structure, enhancing material aggregation at the microscale. Additionally, Cl^- ions modulate local supersaturation and surface charge during hydrothermal growth, which retards growth on specific facets and yields thinner nanosheets that assemble more compactly. Conversely, iodine ions (I^-) have a larger ionic radius (~2.20 Å) and lower electronegativity (2.66), and their weaker complexation/adsorption leads to lower nucleation density and larger nanosheets with more open layer spacing and structural swelling, resulting in a more dispersed morphology. The weaker interaction, also reduces templating/aggregation hindering the formation of tightly clustered nanoflowers. Additionally, the iodine-mediated growth reduces mutual attraction between nanostructures, further contributing to the dispersed morphology. The enhanced interconnection of nanosheets, higher electrochemically accessible surface area, and reduced tortuosity enhance the effective electronic/ionic transport in β-NH.[23,24] Charge transport proceeds *via* redox-coupled polaron hopping through the Ni–O framework; better crystallinity and percolation increase orbital overlap/connectivity, lowering internal resistance. In contrast, poorer interflake connectivity

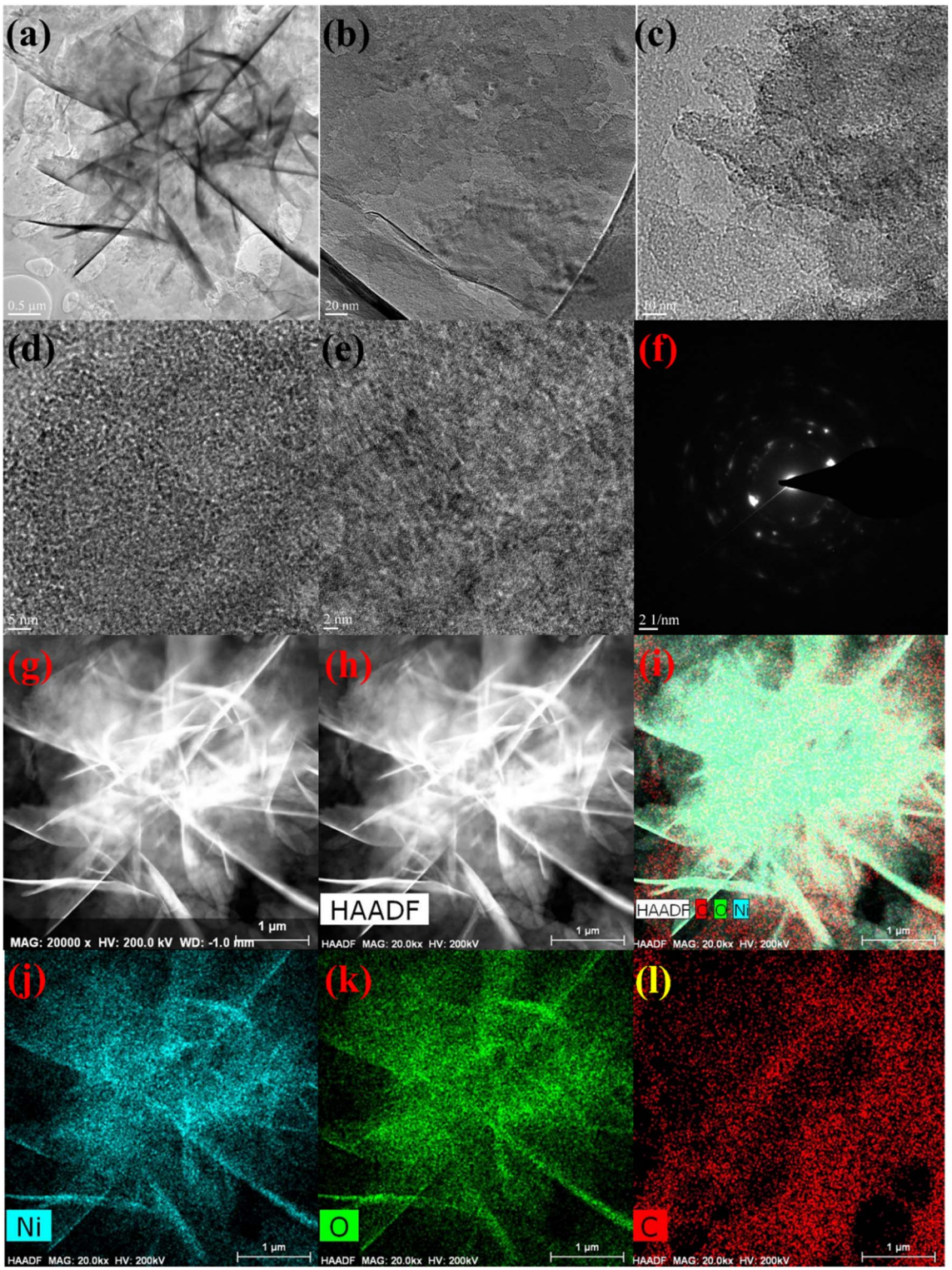

Fig. 4 (a–e) FE-TEM images, (f) SAED pattern, (g and h) bright field scattered images and HAADF, (i) combined mapping elemental image, and (j–l) elemental mapping images of ACl-NH sample.

and higher defect density obstruct. electron pathways and diminishing conductivity. The electrochemical performance of NH is driven by the redox reactions of Ni^{2+}/Ni^{3+}. Higher nickel content increases active sites for these reactions, expediting the electrochemical processes and enabling more uniform electron transfer and ion migration. The oxidation of Ni^{2+} to Ni^{3+} during charging and the subsequent reduction back to Ni^{2+} during discharging contribute to the formation of NiOOH, enhancing the material's activity and specific capacity. Additionally, shorter electron/ion pathways in denser assemblies reduce the

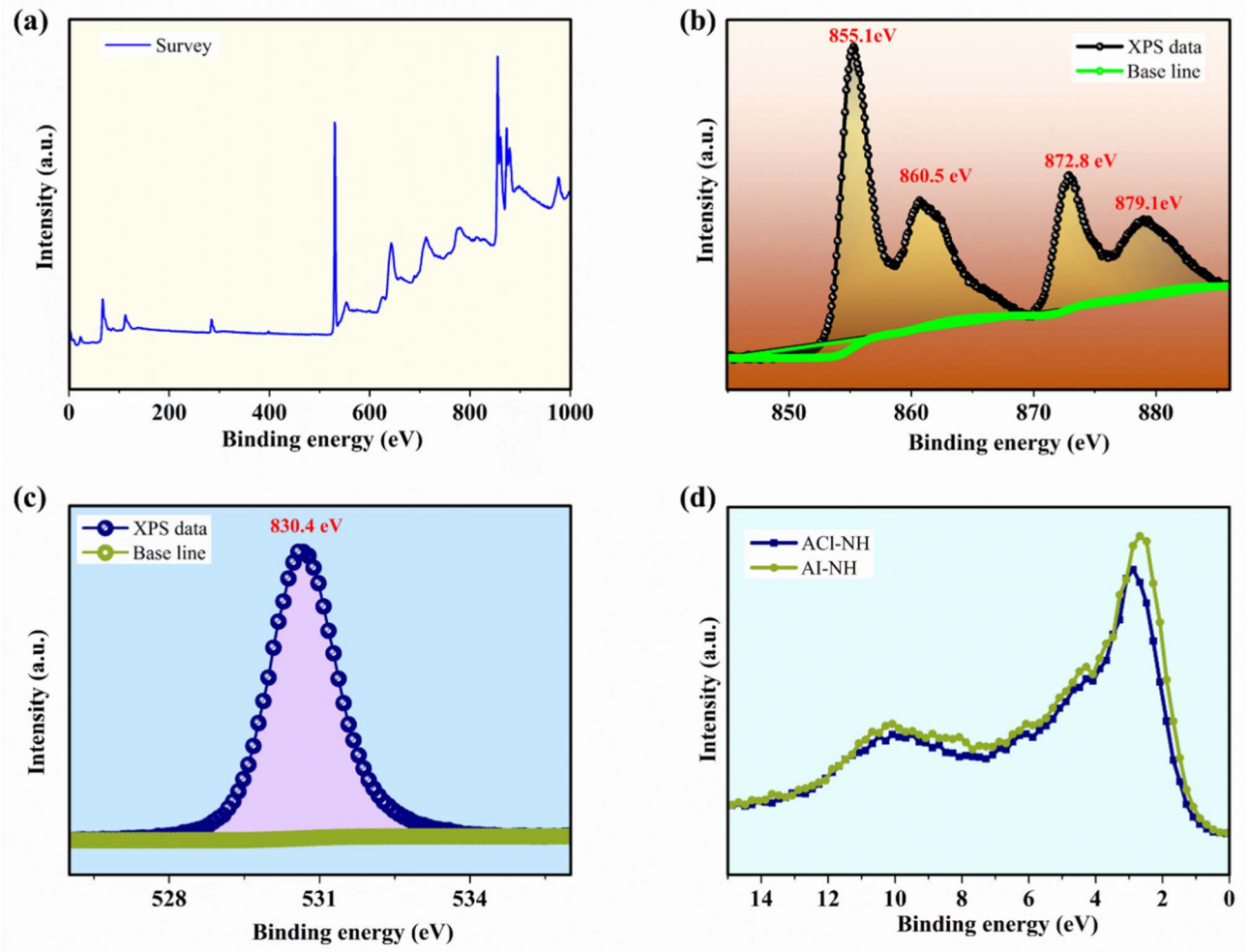

Fig. 5 XPS spectra of (a) survey scan, (b) Ni 2p; and (c) O 1s of ACl-NH sample; (d) valence band spectrum of AI-NH and ACl-NH sample.

distance for charge transfer between neighboring nickel sites, accelerating reaction kinetics. The denser better-connected nanosheet assemblies with improved crystallinity reduce lattice defects and vacancies, accommodating volume changes during charge–discharge cycles and extending the material's cycling lifespan. Furthermore, the β-NH structure with enhanced with improved crystallinity/morphology exhibits greater resistance to phase transitions, ensuring lattice stability and minimizing irreversible damage. This compact arrangement also reduces electrolyte erosion and dissolution losses, contributing to improved cycling stability and material durability.

Fig. 6 presents the surface area and pore size distribution of the ACl-NH and AI-NH samples as determined through BET analysis, which provides critical insights into their structural and adsorption properties. Fig. 6(a and b) depicts the nitrogen adsorption and desorption isotherms for ACl-NH and AI-NH. The isotherms reveal a distinct difference in adsorbate–adsorbent interactions. Notably, the absence of a pronounced knee in the curves for AI-NH indicates extremely weak interactions between the material surface and nitrogen molecules, reflecting a less favorable adsorption environment. The specific areas of ACl-NH and AI-NH were measured to be 16.3 $m^2\ g^{-1}$ and 9.58 $m^2\ g^{-1}$, respectively. The higher surface area of ACl-NH compared to AI-NH highlights its superior adsorption properties, which are critical for enhancing electrochemical performance. In the β-NH crystal structure, Ni^{2+} function as key active sites for redox reactions, while OH^- provide the electrochemical environment. The greater nickel content in ACl-NH contributes to an increased density of active sites, enhancing its capacity for redox reactions. This improvement directly correlates with a higher capacity and overall material efficiency. Additionally, the elevated nickel content in ACl-NH reinforces Ni–OH bonds and reduces lattice defects, resulting in a more ordered and stable crystal structure. This structural order mitigates lattice stress during charge–discharge cycles, improving the material's stability and cycling lifespan. Fig. 6(c and d) present the pore size distribution curves of ACl-NH and AI-NH. The pore size of ACl-NH, at 13.6 nm, is smaller than AI-NH (23.5 nm), contributing to its higher surface area and added active sites for electrochemical responses. This smaller pore size, coupled with uniform distribution, enhances ion adsorption and transport efficiency, making ACl-NH the best-performing material for electrochemical uses.

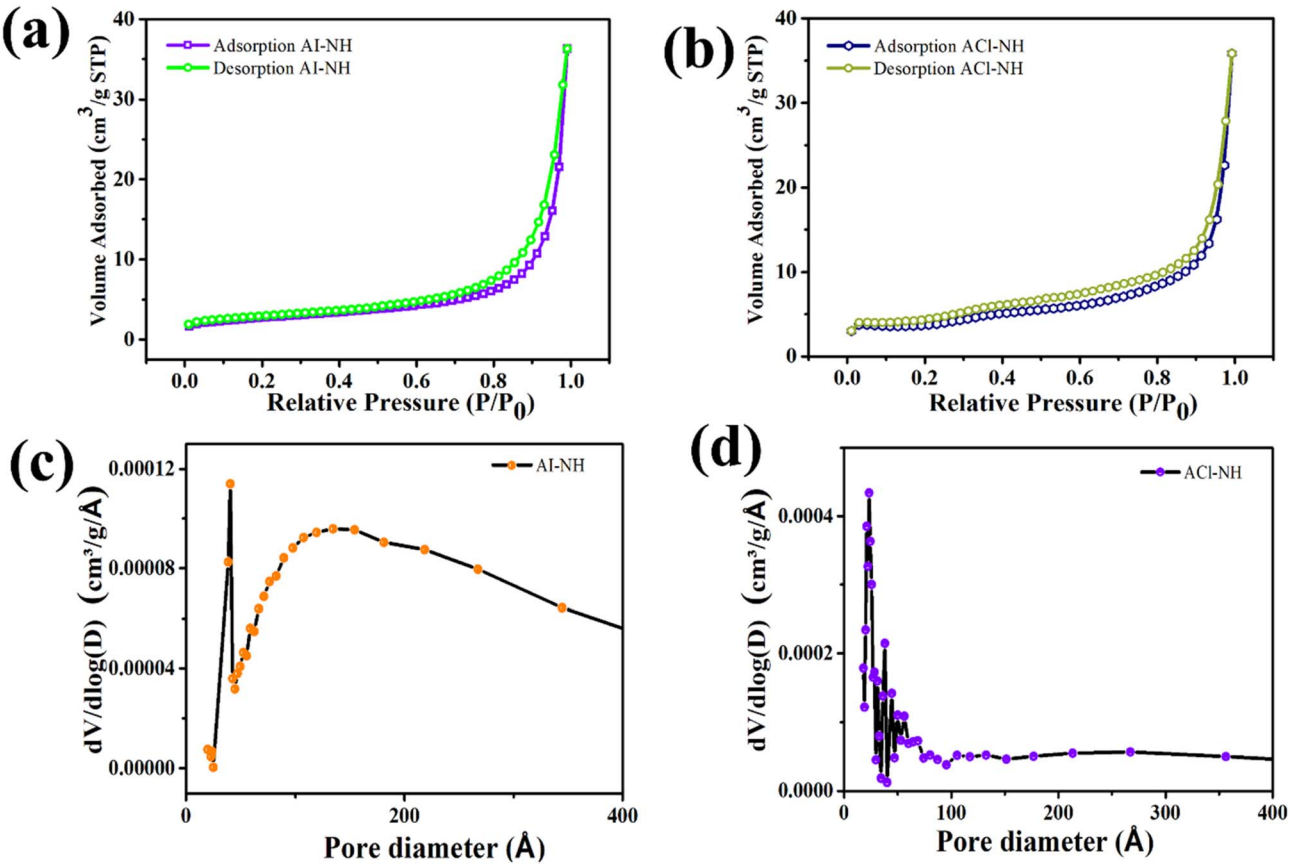

Fig. 6 (a and b) N_2 adsorption and desorption isotherms and (c and d) pore size distribution of AI-NH and ACl-NH samples.

3.3 Electrochemical performances

CV is an essential technique for analyzing the electrochemical characteristics of supercapacitors, providing valuable insights into their charge storage mechanisms, capacitive behavior, and reaction kinetics.[23] Fig. 7 illustrates the CV profiles of AI-NH and ACl-NH electrodes in 1 M KOH at varying scan rates from 0 to 0.6 V. Both samples display similar current responses, which increase with higher scan rates. As depicted in Fig. 7(a and b), the CV curves of both electrodes reveal distinct oxidation and reduction peaks, indicative of pseudocapacitive behavior. However, deviations from the typical "duck-shaped" CV profile are observed, particularly at the reduction and oxidation peak around 0.3 V and 0.4 V, respectively. Fig. 7(c) compares the performances of AI-NH and ACl-NH electrodes, showing that the ACl-NH electrode achieves the highest current response, indicating enhanced charge transfer capability.

The combined analysis of Fig. 8 and 9 highlights the superior electrochemical performance of ACl-NH compared to AI-NH. Specifically, Fig. 8(a–c) consistently show higher peak current values for ACl-NH across identical scan rates. This indicates that ACl-NH exhibits enhanced electrochemical activity and a greater charge storage capacity under equivalent conditions. Additionally, the material demonstrates improved electron and ion transport, contributing to better conductivity and ion diffusion properties. The association between the logarithm of peak current ($\log I_{peak}$) and scan rate ($\log v$) delivers valuable insights into the kinetic behavior of the electrode processes and the underlying energy storage mechanisms. In the logarithmic coordinate system, the association of peak current at scan rate can be expressed as:[23]

$$\log I_p = b \log v + \log(a) \quad (1)$$

The peak current (I_p) is related to the scan rate (v) by a power-law relationship, where b is the slope and a is a constant. The b-values of 0.55 for AI-NH and 0.51 for ACl-NH fall between the ideal values for surface-controlled capacitive processes ($b \approx 1.0$) and diffusion-controlled intercalation processes ($b \approx 0.5$). The slightly higher b-value of AI-NH (0.55) implies a marginally greater contribution from surface-driven capacitive reactions compared to ACl-NH, which could facilitate faster charge transfer at elevated scan rates. Conversely, ACl-NH, with a b-value of 0.51, shows stronger dependence on diffusion-limited kinetics, suggesting that ion transport within the electrode structure governs its rate performance.

Fig. 9 shows the charge-storage contributions of AI-NH and ACl-NH electrodes, separating capacitive and diffusion-controlled processes. Across the tested scan rates, diffusion-driven reactions dominate, particularly at lower sweep rates. As the scan rate rises from 1 mV s^{-1} to 8 mV s^{-1} (Fig. 9(a and b)), the diffusion-controlled share declines noticeably from about

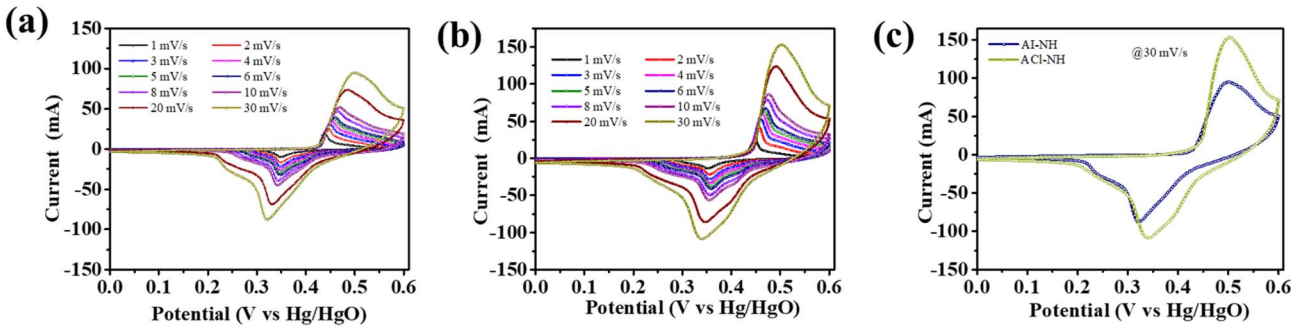

Fig. 7 CV curves for (a) AI-NH, (b) ACl-NH; and (c) comparison of CV curves among pure Ni foam (NF), AI-NH, and ACl-NH.

84.4% to 65.7% for AI-NH and from 92.9% to 82.3% for ACl-NH highlighting the reduced influence of bulk ion transport when the timescale for diffusion becomes limited. At intermediate scan rates (2 mV s^{-1}) (Fig. 9(c and d)), both electrodes display battery-like behavior, where faradaic diffusion remains the principal charge-storage pathway but is complemented by surface-controlled capacitive reactions. This mixed mechanism, with a dominant diffusion component supported by a smaller yet important capacitive share, offers the dual benefit of the high-capacity characteristic of faradaic storage and the high-rate capability associated with capacitive processes.

Fig. 10(a and b) illustrates the potential *versus* time graphs for the AI-NH and ACl-NH electrodes during GCD cycles. These curves represent the variation in potential of the electrodes throughout the charge and discharge processes. Both electrodes demonstrate comparable behavior; however, the discharge time of the ACl-NH electrode is significantly longer than that of the AI-NH electrode, as shown in the comparison of GCD curves in Fig. 10(c). This extended discharge duration suggests an enhanced ability of the ACl-NH electrode to store and release energy, indicative of its superior electrochemical activity. This enhanced performance may be credited to favorable characteristics such as high capacity and low internal resistance.[24–26] The specific capacity values for both electrodes are inversely proportional to the current density, as shown in Fig. 10(d). This trend reflects a charge storage mechanism that combines capacitive behavior with diffusion-limited processes. At 1.5 A g^{-1}, the ACl-NH electrode achieved a capacity of 795 C g^{-1}, outperforming the AI-NH electrode, which recorded a specific capacity of 601.5 C g^{-1}. When the current density was amplified to 4 A g^{-1}, the capacity dropped to 484 C g^{-1} for the ACl-NH electrode and to 276 C g^{-1} for the AI-NH electrode. These results demonstrate the superior ionic and electronic transport properties of the ACl-NH electrode, as evidenced by its consistently higher capacity across all tested current densities. This enhanced electroactivity is likely owing to the electrode's improved surface structure and higher active site availability, which facilitate better charge storage and transfer capabilities compared to the AI-NH electrode.

The Nyquist plots for the AI-NH and ACl-NH electrodes, shown in Fig. 11(a), reveal distinct electrochemical characteristics. The hemispherical arc represents the charge transfer resistance (R_{ct}), which is associated with the resistance encountered during ion transfer or transmission processes within the electrode. In contrast, the linear region at lower frequencies reflects diffusion-controlled processes and may also indicate additional electrochemical phenomena contributing to the overall impedance behavior. The estimated R_{ct} values for the AI-NH and ACl-NH electrodes are 36.82 and 15.21 Ω, respectively. Fig. S1 and Table S1 present the corresponding equivalent circuit along with the extracted EIS fitting parameters. The significantly lower R_{ct} value for the ACl-NH electrode suggests a more efficient ion transfer mechanism compared to the AI-NH electrode. This enhanced ion transfer efficiency could be accredited to the structural and compositional advantages of the ACl-NH electrode, such as improved ionic conductivity,

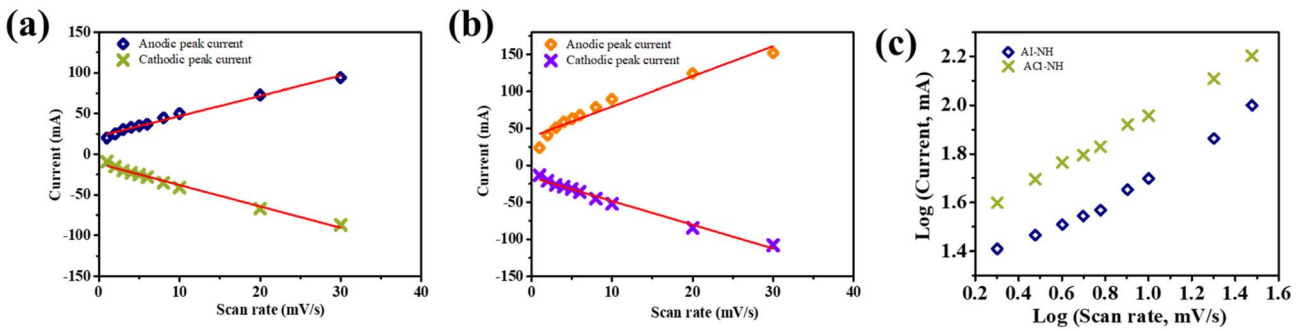

Fig. 8 Peak current *vs.* scan rate for (a) AI-NH, (b) ACl-NH; and (c) comparison of log peak current *vs.* log scan rate for AI-NH and ACl-NH samples.

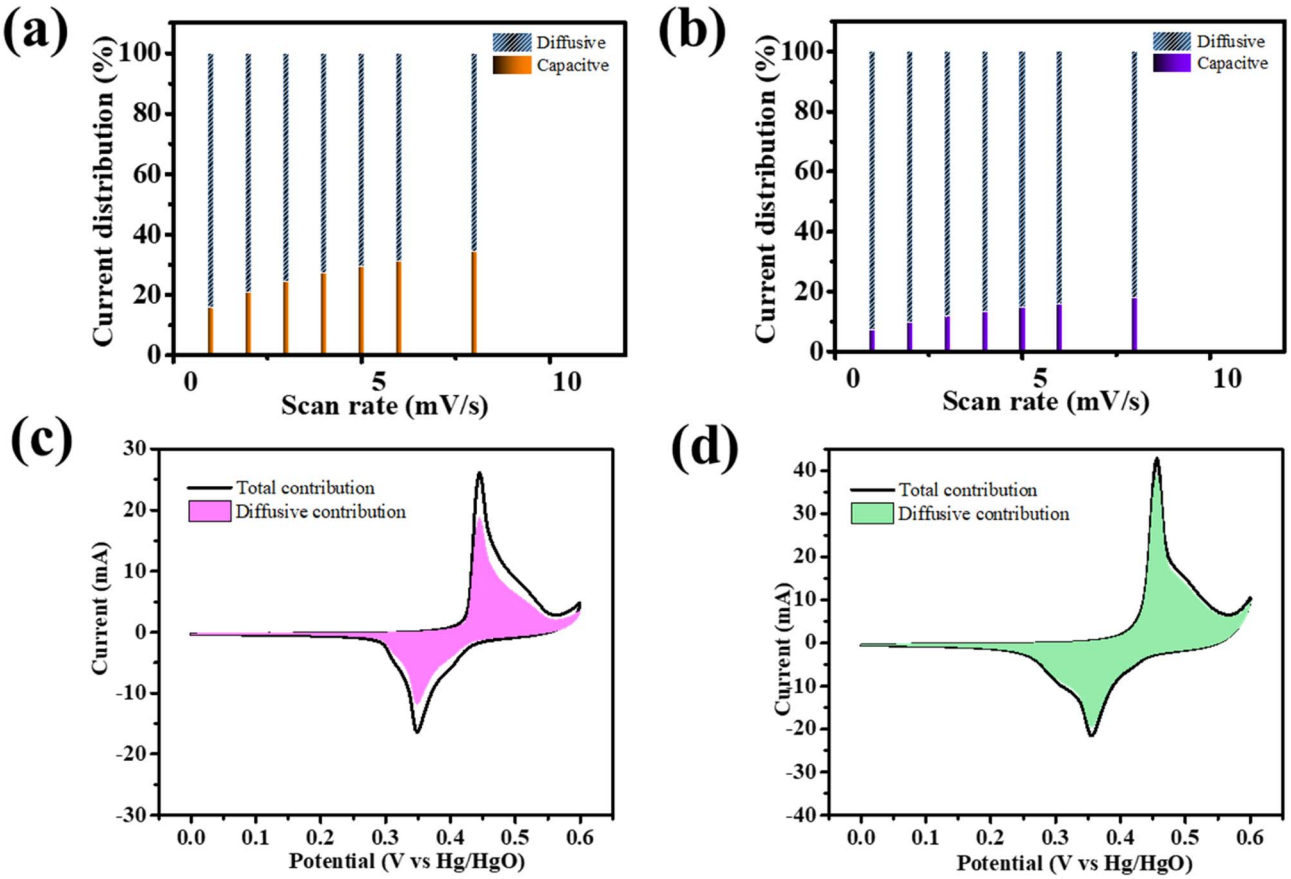

Fig. 9 Total contribution (capacitive + diffusion) for (a) AI-NH and (b) ACl-NH; CV curves showing total contribution and diffusion-controlled mechanisms for (c) AI-NH and (d) ACl-NH samples.

better electrode–electrolyte interface characteristics, and higher surface area with accessible active sites. The reduced resistance in the ACl-NH electrode implies superior electrochemical performance, enabling faster charge and discharge cycles and more efficient energy storage. Fig. 11(b) illustrates the working stability and coulombic competence of the ACl-NH electrode over 6000 cycles. The results indicate minimal capacity degradation throughout the extended cycling process, maintaining nearly 97% retention. This exceptional stability demonstrates the electrode's robust performance and highlights its potential suitability for incorporation into advanced energy storage devices.

3.4 Button-cell asymmetric device (BAD) performance

To further evaluate the practical applicability of the AI-NH and ACl-NH materials, a button-cell asymmetric device (BAD), denoted as AI-NH||ACl-NH, was fabricated. The construction details of the BAD are presented in Fig. 12(a). CV analysis was accomplished at 50 mV s^{-1} across voltage windows, from 0.6 V to 1.6 V (Fig. 12(b)), as well as at varying sweep rates as of 5 mV s^{-1} to 500 mV s^{-1} within a fixed 1.6 V voltage (Fig. 12(c)). The results reveal a minor reduction peak around 1.4 V, with no significant oxidation peak, suggesting weak redox reactions. This indicates that charge storage in the BAD is mixed faradaic/capacitive, with only a small fraction of active sites contributing to pseudocapacitive behavior. Additionally, the device's performance was assessed under current densities from 1.5 A g^{-1} to 4 A g^{-1} (Fig. 12(d)). The estimated capacitance, as shown in Fig. 12(e), decreased from a maximum of 106.5 F g^{-1} at 1.5 A g^{-1} to approximately 40 F g^{-1} at 4 A g^{-1}, reflecting the dependency of capacitance *vs.* current density. Fig. 13(a and b) demonstrates the excellent energy and power densities of the BAD, delivering 37.8 Wh kg^{-1} and 1975.3 W kg^{-1}, correspondingly, with a discharge time of 69 seconds at 1.5 A g^{-1}. As shown in the Nyquist plot (Fig. 13(c)), the estimated R_s and R_{ct} values for BAD are 1.35 and 106 Ω, respectively. Additionally, the near-vertical line in the low-frequency region confirms ideal capacitive behavior and efficient ion diffusion. Together, these features demonstrate the device's excellent electrochemical performance, driven by its optimized conductivity and fast charge transport capabilities. Fig. 13(d) highlights the cycling stability of the BAD, tested over 8500 cycles at 13.6 A g^{-1}. The device demonstrates remarkable stability, retaining 78% of its initial specific capacitance even after prolonged cycling, further emphasizing its durability and suitability for advanced storage uses.

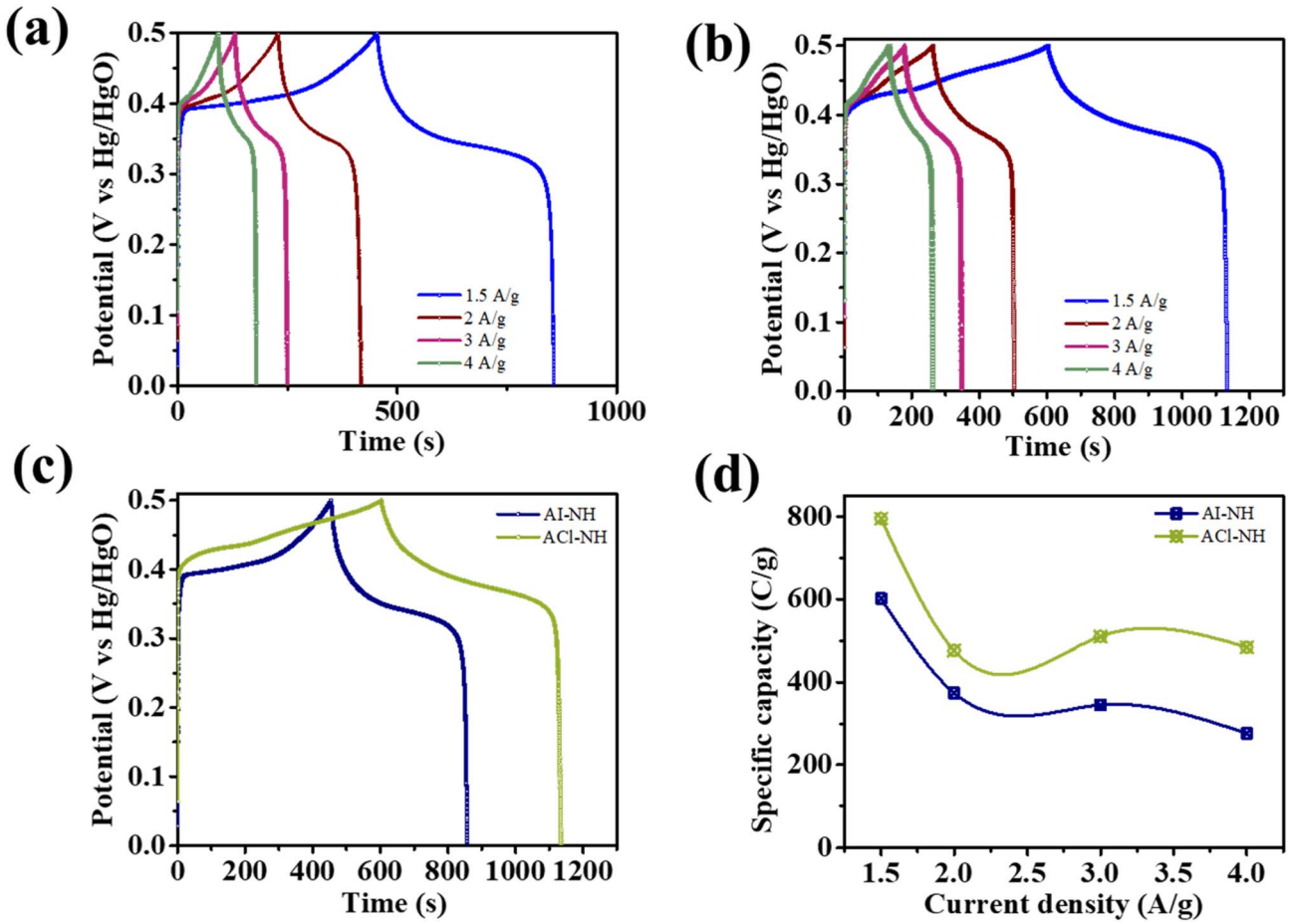

Fig. 10 GCD curves for (a) AI-NH, (b) ACl-NH; (c) comparison of GCD curves among pure Ni foam (NF), AI-NH, and ACl-NH; and (d) specific capacity *vs.* current densities for AI-NH and ACl-NH samples.

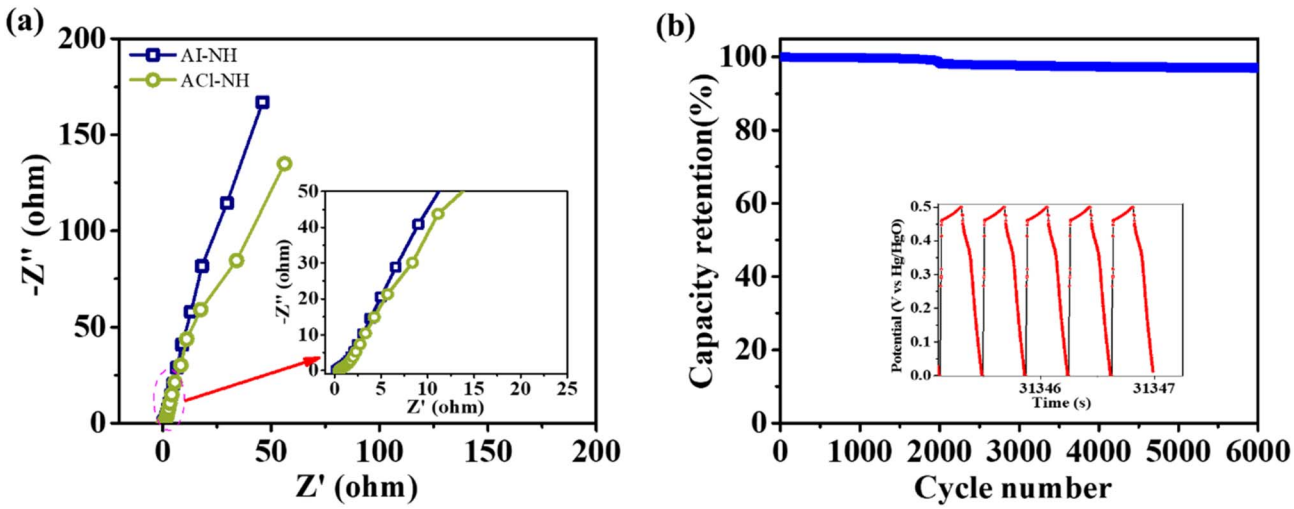

Fig. 11 (a) EIS spectra of AI-NH and ACl-NH electrodes and (b) cycling stability of ACl-NH electrode [inset displays the corresponding GCD curves for the final few cycles @ 24 A g^{-1}].

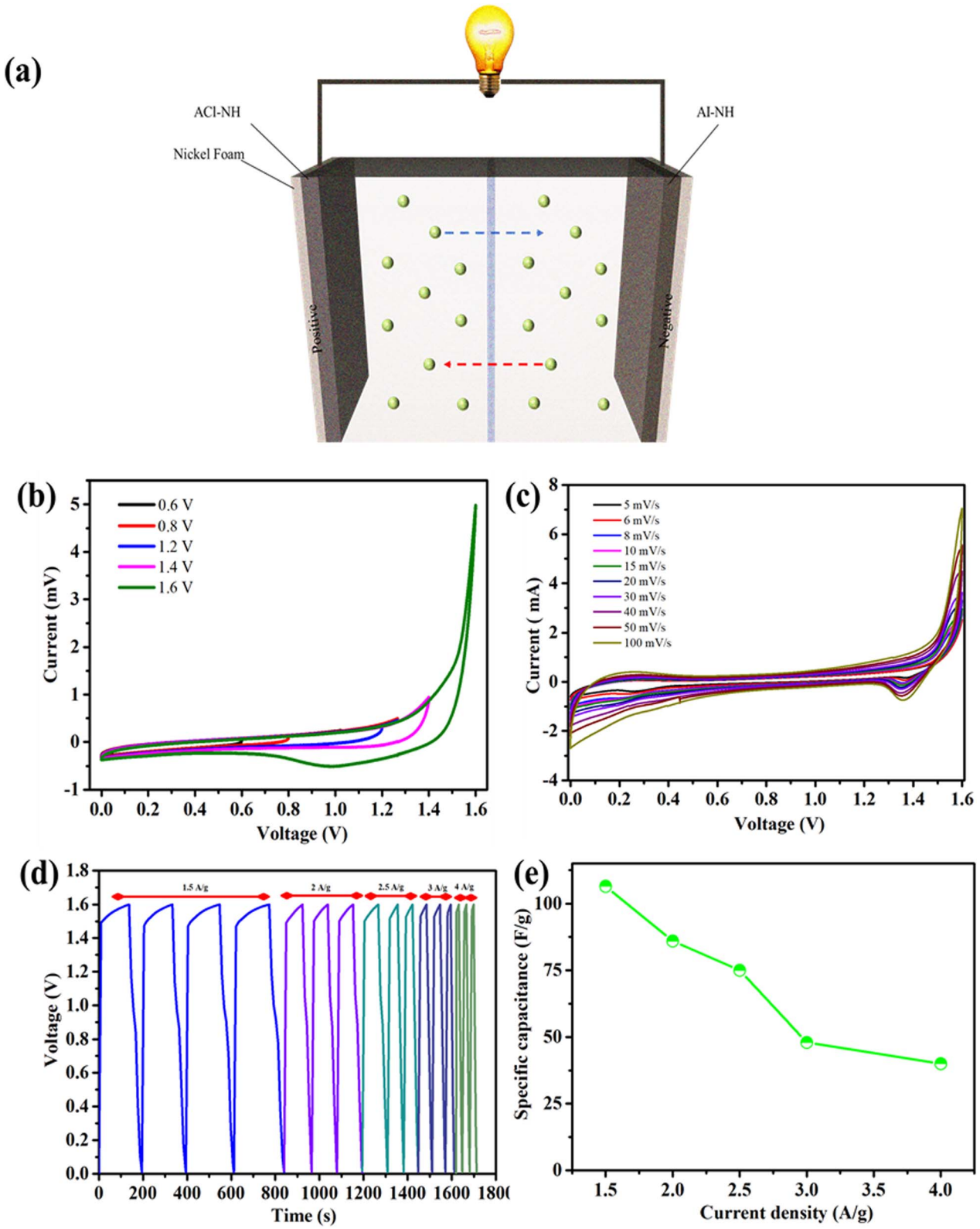

Fig. 12 Two-electrode device: (a) construction of BADs, CV profiles (b) at different potentials, (c) at different scan rates, (d) GCD curves at different current densities, and (e) specific capacitance *vs.* current densities.

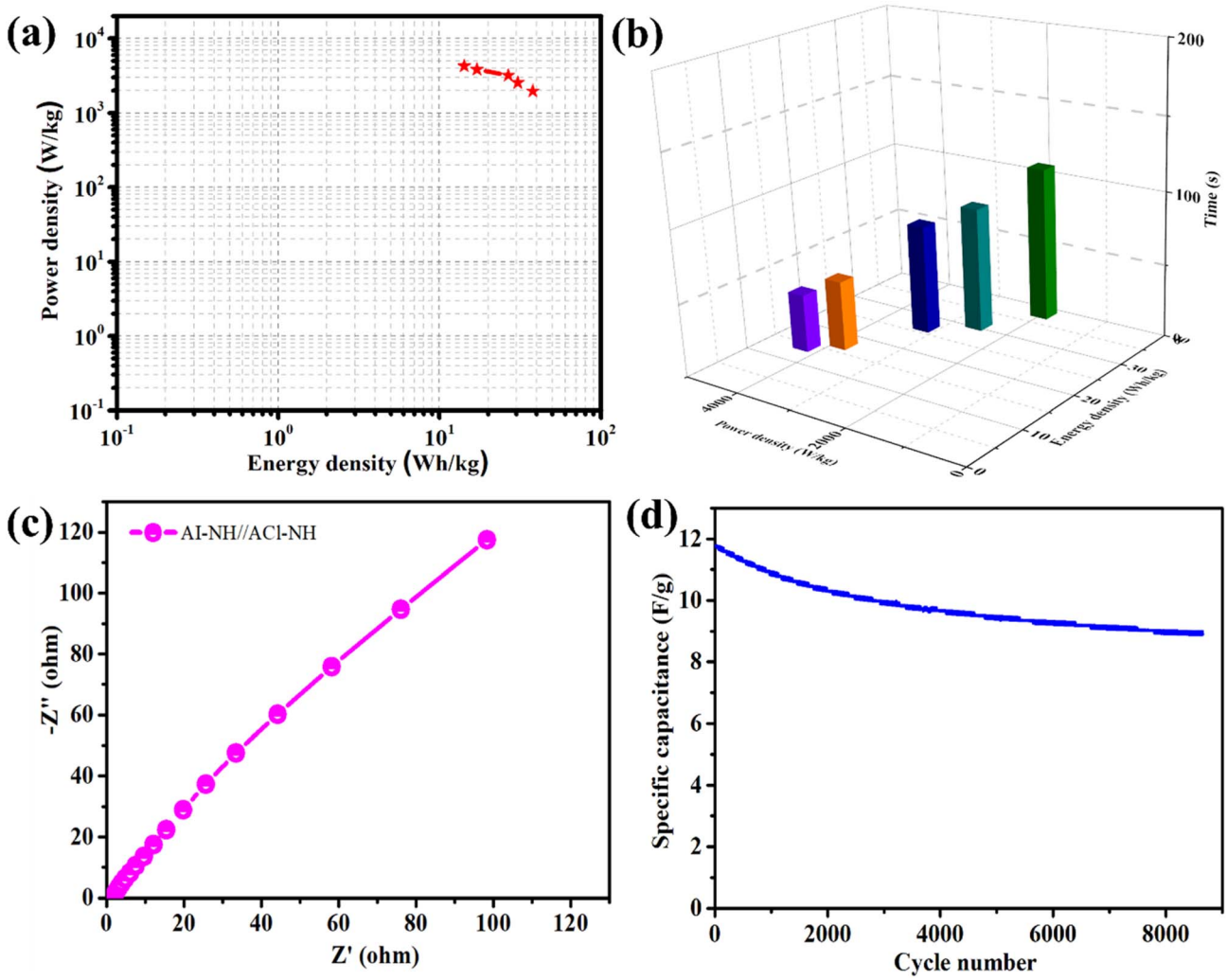

Fig. 13 (a) Energy density *vs.* power density, (b) energy density *vs.* power density *vs.* discharge, (c) Nyquist plot and (d) cycling stability of AI-NH||ACl-NH SSDs.

4. Conclusions

This research explores the effectiveness of using halogen-based precursors to synthesize double-layered nickel hydroxides (NH) for energy storage devices. The study confirms that halogen ions play a critical role in shaping the morphology, surface characteristics, and electrochemical properties of AI-NH and ACl-NH electrodes. Notably, the ACl-NH electrode demonstrated superior performance, reaching a specific capacity of 795 C g^{-1} at 1.5 A g^{-1} and maintaining 97% of its capacity after 6000 cycles. This enhanced activity is attributed to its increased surface area and refined structure, which promote efficient ion and electron movement. Performance testing of a asymmetric button-cell device constructed with AI-NH and ACl-NH electrodes further validated these results, delivering a capacitance of 106.5 F g^{-1} at 1.5 A g^{-1}, an energy density of 37.8 Wh kg^{-1} at 1975.3 W kg^{-1}, with 78% capacitance retention over 8500 cycles. These outcomes emphasize the impact of halogen-assisted morphological tuning on improving electrode efficiency. Overall, this study delivers valuable guidance for designing high-performance, long-lasting electrodes through strategic precursor selection for future supercapacitor uses.

Conflicts of interest

There are no conflicts to declare.

Data availability

The datasets used in this study are available from the corresponding author (S. V. Prabhakar Vattikuti) upon request.

Supplementary information (SI): details of characterization, electrochemical test procedures, electrolyte preparation and device making procedures. See DOI: **https://doi.org/10.1039/d5na00488h**.

Acknowledgements

This work was financially supported by the National Research Foundation of Korea (number: RS-2023-00280665). Natural Science Foundation of Hubei Province (no. 2024AFB376), Science and Technology Research Project of Education Department of Hubei Province (Q20232701), Xiaogan City Natural Science Plan Project (XGKJ2023010056).

References

1 S. Natarajan, M. Ulaganathan and V. Aravindan, Building next-generation supercapacitors with battery type $Ni(OH)_2$, *J. Mater. Chem. A*, 2021, **9**, 15542–15585.

2 X. R. Yi, V. Celorrio, H. Y. Zhang, N. Robertson and C. Kirk, α/β-$Ni(OH)_2$ phase control by F-ion incorporation to optimise hybrid supercapacitor performance, *J. Mater. Chem. A*, 2023, **11**, 22275–22287.

3 X. R. Yi, H. P. Sun, N. Robertson and K. Kirk, Nanoflower $Ni(OH)_2$ grown in situ on Ni foam for high-performance supercapacitor electrode materials, *Sustainable Energy Fuels*, 2021, **5**, 5236–5246.

4 S. A. Mozaffari, S. H. M. Najafi and Z. Norouzi, Hierarchical NiO@$Ni(OH)_2$ nanoarrays as high-performance supercapacitor electrode material, *Electrochim. Acta*, 2021, **368**, 137633.

5 J. B. Li, Y. Liu, W. Cao and N. Chen, Rapid in situ growth of β-$Ni(OH)_2$ nanosheet arrays on nickel foam as an integrated electrode for supercapacitors exhibiting high energy density, *Dalton Trans.*, 2020, **49**, 4956–4966.

6 V. Butera and M. C. Toroker, Electronic properties of pure and Fe-doped β-$Ni(OH)_2$: New insights using density functional theory with a cluster approach, *J. Phys. Chem. C*, 2016, **120**, 12344–12350.

7 S. Natarajan, M. Ulaganathan and V. Aravindan, Building next-generation supercapacitors with battery type $Ni(OH)_2$, *J. Mater. Chem. A*, 2021, **9**, 15542–15585.

8 J. Z. Yin, G. L. Zhou, X. L. Gao, J. Chen, L. Zhang, J. Xu, P. Zhao and F. Gao, α- and β-phase Ni-Mg hydroxide for high performance hybrid supercapacitors, *Nanomaterials*, 2019, **9**, 1686.

9 T. T. B. Tran, E. J. Park and J. T. Son, Optimization of hydrothermal synthesis of nickel oxide with flower-like structure, *Korean J. Chem. Eng.*, 2024, **41**, 473–478.

10 N. A. Hoque, P. Thakur, A. Kool, S. Das and P. P. Ray, Optical and dielectric properties of hydrothermally synthesized $Ni(OH)_2$ nanoparticles: a morphology and size dependent study, *J. Mater. Sci.: Mater. Electron.*, 2017, **28**, 5375–5383.

11 L. Ping, G. E. Minarik, H. Gao, J. Cao, T. Li, H. Kitadai and X. Ling, Synthesis of 2D layered transition metal (Ni, Co) hydroxides via edge-on condensation, *Sci. Rep.*, 2024, **14**, 3817.

12 J. Yu, S. Pan, Y. Zhang, Q. Liu and B. Li, Facile synthesis of monodispersed α-$Ni(OH)_2$ microspheres assembled by ultrathin nanosheets and its performance for oxygen evolution reduction, *Front. Mater.*, 2019, **6**, 124.

13 C. Ouyang, X. Wang, C. Wang, Z. Zhang, J. Wu, Z. Ma, S. Dou and S. Wang, Hierarchically porous Ni_3S_2 nanorod array foam as highly efficient electrocatalyst for hydrogen evolution reaction and oxygen evolution reaction, *Electrochim. Acta*, 2015, **174**, 297–301.

14 H. Zhang, B. Xu, Z. Xiao, H. Mei, L. Zhang, Y. Han and D. Sun, Optimizing crystallinity and porosity of hierarchical $Ni(OH)_2$ through conformal transformation of metal–organic framework template for supercapacitor applications, *CrystEngComm*, 2018, **20**, 4313–4320.

15 S. Liu, S. C. Lee, U. Patil, I. Shackery, S. Kang, K. Zhang, J. H. Park, K. Y. Chung and S. C. Jun, MnCo-layered double hydroxides@$Ni(OH)_2$ core–shell heterostructures as advanced electrodes for supercapacitors, *J. Mater. Chem. A*, 2017, **5**, 1043–1049.

16 J. Yan, Z. Fan, W. Sun, G. Ning, T. Wei, Q. Zhang, R. Zhang, L. Zhi and F. Wei, Advanced asymmetric supercapacitors based on $Ni(OH)_2$/graphene and porous graphene electrodes with high energy density, *Adv. Funct. Mater.*, 2021, **22**, 2632–2641.

17 E. K. Andreou, I. Vamvasakis and G. S. Armatas, Fabrication of high-surface-area mesoporous frameworks of β-Ni $(OH)_2$–$CdIn_2S_4$ p–n nano-heterojunctions for improved visible light photocatalytic hydrogen production, *Inorg. Chem. Front.*, 2024, **11**, 5273–5285.

18 M. Aghazadeh, A. N. Golikand and M. Ghaemi, Synthesis, characterization, and electrochemical properties of ultrafine β-$Ni(OH)_2$ nanoparticles, *Int. J. Hydrogen Energy*, 2011, **36**, 8674–8679.

19 X. Yi, V. Celorrio, H. Zhang, N. Robertson and C. Kirk, α/β-Ni $(OH)_2$ phase control by F-ion incorporation to optimise hybrid supercapacitor performance, *J. Mater. Chem. A*, 2023, **11**, 22275–22287.

20 S. Wang, C. Tan, L. Fei, H. Huang, S. Zhang, H. Huang, X. Zhang, Q. Huang, Y. Hu and H. Gu, Rational design and in-situ synthesis of ultra-thin β-Ni $(OH)_2$ nanoplates for high performance all-solid-state flexible supercapacitors, *Front. Chem.*, 2020, **8**, 602322.

21 D. Wang, B. Guan, Y. Li, D. Li, Z. Xu, Y. Hu, Y. Wang and H. Zhang, Morphology-controlled synthesis of hierarchical mesoporous α-$Ni(OH)_2$ microspheres for high-performance asymmetric supercapacitors, *J. Alloys Compd.*, 2018, **737**, 238–247.

22 J. Hao, L. Yan, L. Luo, Q. Liu, Y. Bai, Y. Han, Y. Zhou, X. Zou and B. Xiang, Halogen chlorine triggered oxygen vacancy-rich Ni $(OH)_2$ with enhanced reaction kinetics for pseudocapacitive energy storage, *J. Energy Chem.*, 2023, **82**, 296–306.

23 J. Hao, L. Yan, X. Zou, Y. Bai, Y. Han, C. Zhu, Y. Zhou and B. Xiang, Series of halogen engineered $Ni(OH)_2$ nanosheet for pseudocapacitive energy storage with high energy density, *Small*, 2023, **19**, 2300467.

24 Z. Song, Q. Yin, S. Yang, Y. Miao, Y. Wu, Y. Z. Li, T. Ren, Y. Sui, J. Qi and J. Han, A high-nickel layered double hydroxides cathode boosting the rate capability for chloride ion batteries with ultralong cycling life, *Small*, 2023, **19**, 2302896.

25 M. Wang, Y. Ni, L. Cao, D. Zhao and X. Ma, Porous Ni/β-Ni $(OH)_2$ superstructures: rapid solvothermal synthesis, characterization, and electrochemical property, *J. Colloid Interface Sci.*, 2013, **401**, 8–13.

26 T. S. Mathis, N. Kurra, X. Wang, D. Pinto, P. Simon and Y. Gogotsi, Energy storage data reporting in perspective—guidelines for interpreting the performance of electrochemical energy storage systems, *Adv. Energy Mater.*, 2019, **9**, 1902007.